Atomic origins of water-vapour-promoted alloy oxidation

Langli Luo [1,7], Mao Su [2,3,4,7], Pengfei Yan [1,7], Lianfeng Zou[5], Daniel K. Schreiber[6], Donald R. Baer[1], Zihua Zhu[1], Guangwen Zhou [5], Yanting Wang [3,4], Stephen M. Bruemmer[6], Zhijie Xu[2]* and Chongmin Wang [1]*

The presence of water vapour, intentional or unavoidable, is crucial to many materials applications, such as in steam generators, turbine engines, fuel cells, catalysts and corrosion[1-4]. Phenomenologically, water vapour has been noted to accelerate oxidation of metals and alloys[5,6]. However, the atomistic mechanisms behind such oxidation remain elusive. Through direct in situ atomic-scale transmission electron microscopy observations and density functional theory calculations, we reveal that water-vapour-enhanced oxidation of a nickel–chromium alloy is associated with proton-dissolution-promoted formation, migration, and clustering of both cation and anion vacancies. Protons derived from water dissociation can occupy interstitial positions in the oxide lattice, consequently lowering vacancy formation energy and decreasing the diffusion barrier of both cations and anions, which leads to enhanced oxidation in moist environments at elevated temperatures. This work provides insights into water-vapour-enhanced alloy oxidation and has significant implications in other material and chemical processes involving water vapour, such as corrosion, heterogeneous catalysis and ionic conduction.

Many oxidation mechanisms, either based on microstructure or atomic defect structure of the growing oxide layer, have been proposed to account for the effect of water vapour on oxidation[7-11]. However, these mechanisms typically are deduced from steady-state oxide growth kinetics and lack direct observations of structural evolution during oxidation, especially at the atomic scale. A mechanistic understanding of the effect of water vapour on alloy oxidation requires knowledge of the defect structure in the growing oxide, where real-time atomic-scale observations under relevant conditions are needed. Aberration-corrected environmental transmission electron microscopy (ETEM) provides an ideal platform for atomic-scale direct observation of structural evolution of materials under dynamic reaction conditions as demonstrated in early-stage oxidation[12-14], catalyst studies[15-17], and crystal interactions in hydrated environments[18]. Here, we use in situ ETEM to examine at the atomic level the oxidation process of a model single-crystalline Ni–10at%Cr alloy film in oxygen.both pure oxygen and water vapour at elevated temperature. The captured atomic-level dynamic process of the oxide layer growth provides insight into how water vapour modifies the oxidation process when compared with oxygen.

The atomic process of NiO formation on the alloy in the case of both O_2 and H_2O are illustrated by two series of in situ high-resolution (HR)TEM images (Supplementary Videos 1 and 2) shown in Fig. 1a,b. These images depict the growth of cuboid NiO crystals on a Ni–Cr alloy surface during oxidation at 1×10^{-6} mbar and 350 °C in O_2 and H_2O, respectively. The experimental details are described in the Methods. The NiO similarly develops in both O_2 and H_2O by a layer-by-layer growth process via the adatom mechanism[19] (shown in Fig. 1a), where the Ni and O atoms diffuse to the reaction front (surface step edges indicated by white arrows in Fig. 1a,b and Supplementary Video 1) forming the NiO lattice layer-by-layer. Typically, following 68 s oxidation in O_2, the lateral size of the NiO crystal (Fig. 1a) increases from 6.8 nm to 7.4 nm, corresponding to three layers of NiO lattice along the [010] direction.

Compared with O_2, a significant feature of the oxidation process in H_2O is the formation of vacancy clusters and their dynamic behaviour in the NiO, as illustrated by the distinct phase contrast (white dashed circles in Fig. 1b) on the square lattice of NiO and confirmed by the simulated HRTEM image (Supplementary Fig. 1). These vacancy clusters are subnanometre cavities formed by incorporating both Ni and O vacancies. The dynamic evolution of the vacancy clusters in the growing oxide (Supplementary Fig. 2) features three characteristics: (1) migration; (2) increasing in size; and (3) annihilation. The vacancy clusters typically grow from a lateral dimension of 1 or 2 NiO(200) atomic layers ($a_{NiO(200)} = 2.08$ Å) to 4 or 5 NiO(200) atomic layers (indicated by white arrows in Supplementary Fig. 3). Such growth process can be accomplished by either absorbing vacancies or merging with other vacancy clusters. The vacancy cluster can be annihilated by migrating to the oxide surface (Fig. 1b). For example, at 0 s, a vacancy cluster with a lateral size of ~3 NiO(200) atomic layers is seen near the oxide surface (Fig. 1b, indicated by the yellow arrow). With continued oxidation, this vacancy cluster migrates to the surface and creates a surface pit (yellow arrow) after 174 s. This surface pit subsequently fills up via adatom diffusion and growth, which leads to a flat surface after 301 s. The dynamic structural evolution of the nanocavites is mediated by the atomic ledge migration, indicating the simultaneous migration and involvement of both Ni and O vacancies in the lattice of NiO.

Accompanying the surface annihilation of the vacancy cluster is a sharp decrease in the number density and the total coverage
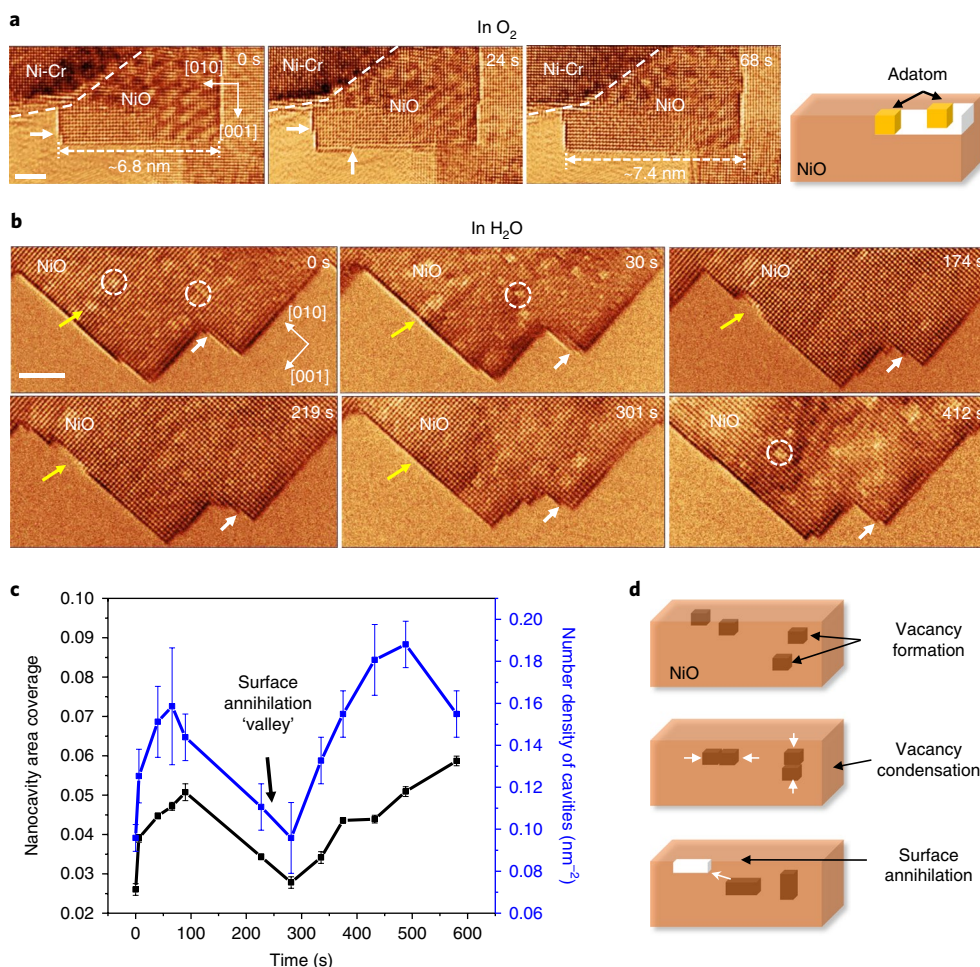
Fig. 1 | In situ observation of dynamic growth of oxides on the Ni–Cr alloy in O₂ and H₂O. a,b, Time-resolved HRTEM images reveal the growth of an initial NiO crystal on the alloy surface in O_2 (**a**) and H_2O (**b**) with $p = 1 \times 10^{-6}$ mbar and $T = 350$ °C. NiO growth proceeds by the adatom-induced, layer-by-layer growth mechanism, which is observed for both cases of oxidation in O_2 and H_2O and is illustrated in the far-right schematic in **a**. The white arrows in **a** and **b** indicate the step edges, which are the reaction front. The oxide formed in O_2 shows no vacancy formation, while the oxide formed in H_2O involves vacancy dynamics. The yellow arrows in **b** track migration of a vacancy cluster towards the surface, leading to the formation of step edges and subsequent annihilation by the adatom mechanism. Scale bars, 1 nm (**a**); 2 nm (**b**). **c**, The plot of the projected area coverage and the number density of the vacancy clusters as a function of time during in situ oxidation in H_2O, featuring a 'valley' related to the surface annihilation event of vacancy clusters. **d**, Schematics of vacancy cluster dynamics.

(projected) of the vacancy clusters before they both quickly recover (Fig. 1c), indicating that for small-sized NiO (~10 nm), the density of the vacancy clusters is highly affected by this surface annihilation event. The vacancy cluster density fluctuation is related to two counterbalancing factors: (1) vacancy-supersaturation-induced nucleation and growth of the vacancy cluster, corresponding to the 'peak' of the number density of vacancy clusters in Fig. 1c; and (2) migration and surface annihilation of the vacancy cluster that leads to the decrease of the number density of vacancy clusters (corresponding to the 'valley' in Fig. 1c). This process repeats as oxidation progresses. The observations described above are schematically illustrated in Fig. 1d, depicting the vacancy dynamics that includes formation, condensation and annihilation in the growing NiO crystals on the Ni–Cr alloy surface during oxidation in H_2O, which is not observed during the growth of NiO in pure O_2. These distinctive microstructural differences are also observed for the oxidation at gas pressure of 1×10^{-2} and 1×10^{-4} mbar (Supplementary Figs. 17 and 18). Hence, the vacancy formation and migration in growing NiO in H_2O indicates a modified oxidation mechanism as compared with that in pure O_2.

During the oxidation by water vapour, H_2O molecules can be easily adsorbed and chemically dissociated into OH^- and H^+ on the NiO surface, and the O–H bonds can be further broken to form free oxygen ions to serve as the oxidizing species[20]. In accordance with previous theoretical prediction[21] and our density functional theory (DFT) calculations, H^+ can penetrate the NiO lattice by overcoming a small diffusion barrier of ~0.35 eV, leading to the formation of interstitial protons, $H_i^{\cdot}$, in the NiO lattice. Based on this physical picture, DFT calculations will provide insight into identifying the role of $H_i^{\cdot}$ defects on the observed formation and clustering process of both O and Ni vacancies. As a representative case, Fig. 2a is a schematic model that illustrates the Ni vacancy formation and clustering in NiO with the presence of $H_i^{\cdot}$. The electron density maps (Fig. 2b) correspond to cases of a perfect NiO crystal and a NiO crystal with one $H_i^{\cdot}$ before and after a Ni vacancy forms at the location near $H_i^{\cdot}$. Similar calculations are also conducted for an O vacancy (Supplementary Table 1). These calculations demonstrate that with respect to perfect NiO crystals, the existence of $H_i^{\cdot}$ decreases the respective formation energies of Ni and O vacancies by 2.83 eV (Fig. 2c) and 1.93 eV (Supplementary Table 1). This means that in
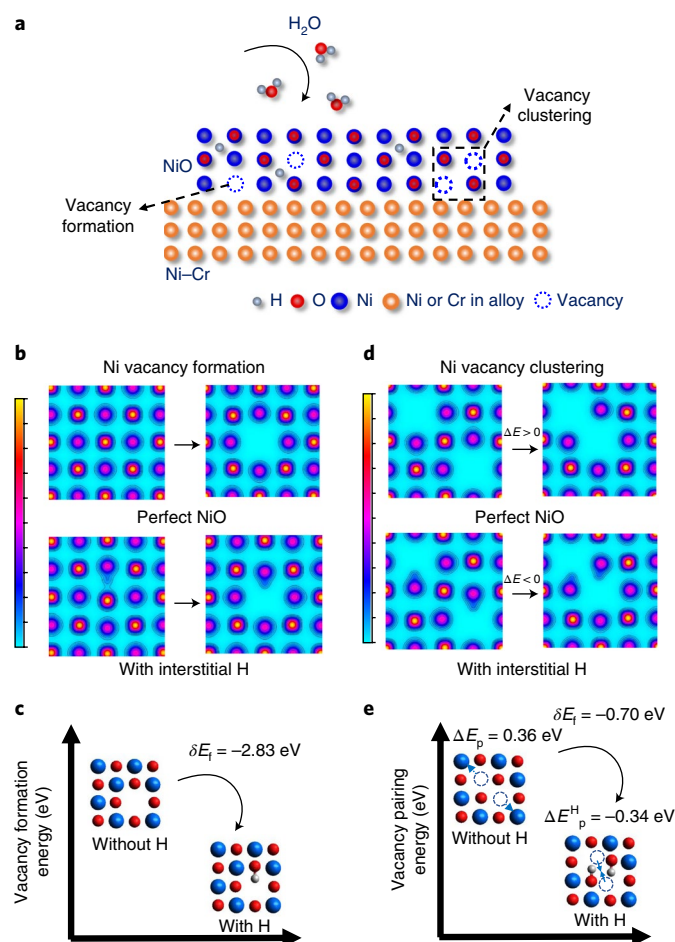
Fig. 2 | Defect-dependent vacancy formation and clustering. a, Schematic of the atomic processes in the oxidation of Ni–Cr alloy in water vapour, illustrating at the atomic level that water vapour enhances vacancy formation and promotes vacancy clustering. **b**, Electron density maps of the NiO lattice with and without the interstitial $H_i^{\cdot}$ in the event of an Ni vacancy formation. **c**, DFT calculation results, showing that vacancy formation energy decreases by 2.83 eV in the presence of an $H_i^{\cdot}$. **d**, Comparison of electron density maps of NiO with and without the interstitial $H_i^{\cdot}$ for the case of two separate Ni vacancies and two adjacent Ni vacancies. **e**, DFT calculation results, showing that in NiO the combination of two separated vacancies leads to an increase of energy of 0.36 eV; while if $H_i^{\cdot}$ is present, the combination of two separated vacancies leads to a decrease of energy of 0.34 eV, revealing that when there is no $H_i^{\cdot}$ in the NiO lattice, the Ni vacancies will remain separated as a stable configuration ($\Delta E > 0$), but if there is $H_i^{\cdot}$, the vacancies will tend to combine to form vacancy pairs ($\Delta E < 0$). E_f is the formation energy of a vacancy, E_p is the energy of a vacancy pair. Similar results are also obtained for the case of O vacancies and are detailed in the Supplementary Information.

the presence of interstitial proton defects, vacancy formation is a thermodynamically favourable process that creates a large number of Ni and O vacancies.

The presence of $H_i^{\cdot}$ not only enhances the generation of Ni and O vacancies, but also affects vacancy stability, which can be assessed from the point of view of vacancy condensation behaviour observed for NiO grown in H_2O (Fig. 1b). The electron density map with a Ni vacancy pair (two adjacent vacancies), representing the presence and absence of $H_i^{\cdot}$, is plotted in Fig. 2d. Correspondingly, the energy change associated with the merging of two Ni vacancies is calculated. In pure NiO, the energy change for the merging of two Ni vacancies is 0.36 eV for spin parallel and

0.18 eV for spin antiparallel. However, incorporating $H_i^{\cdot}$ defects in the NiO lattice alters the energy change for merging of two Ni vacancies, resulting in −0.34 eV for spin parallel and −0.35 eV for spin antiparallel. This means that in pure NiO, two adjacent Ni vacancies repel each other, and the individual vacancies are more energetically stable than when they merge together to form a vacancy cluster. In contrast, with the presence of $H_i^{\cdot}$, vacancy clustering is energetically favoured (Fig. 2e). Similar results are also obtained for O vacancies and their pairing (Supplementary Table 1). Hence, along with Ni–Ni and O–O vacancy pair formation, it is anticipated that Ni and O vacancies can merge together to form vacancy clusters. This is in accordance with our experimental results, showing that vacancy clusters are constantly generated and condensed throughout the oxidation process in water vapour. The DFT calculation results at 0 K are also validated by considering the entropy contributions to the total energy change at elevated temperature used in our experiments as detailed in the Supplementary Information.

The presence of $H_i^{\cdot}$ in the NiO lattice also leads to lowering of diffusion barriers of both Ni and O in NiO and, therefore, enhances ion migration. Figure 3a shows that for $H_i^{\cdot}$-mediated Ni diffusion, the diffusion barrier is 0.48 eV, which, in contrast, is 1.44 eV for Ni diffusion in NiO. Similar results are also obtained for the case of $H_i^{\cdot}$-mediated O diffusion in NiO (summarized in Supplementary Table 2). Hence, both Ni and O diffusion are enhanced by the presence of $H_i^{\cdot}$ defects, which, consequently, leads to an increased oxidation rate for the case of water vapour versus that of pure oxygen. Although the equilibrium concentration of $H_i^{\cdot}$ in NiO can decrease with increasing temperature due to entropy loss through proton dissolution, the non-equilibrium oxidation process still can dynamically generate considerable amounts of proton defects in the NiO. Correspondingly, a few protons could catalyse the vacancy migrations of both Ni and O.

NiO growth is dominated by the through-lattice diffusion of both Ni and O in the NiO lattice, which is significantly affected by the vacancies in the NiO. The presence of $H_i^{\cdot}$ lowers the diffusion barriers of Ni and O as discussed above. Our atomic-scale experimental and theoretical studies of the effect of water vapour on defect formation and evolution in NiO during the initial oxide growth are consistently supported by the microscale structural evolution of oxides. The scanning (S)TEM high-angle annular dark-field (HAADF) images in Fig. 3b,c reveal the morphology of an oxidizing Ni–Cr surface in O_2 and H_2O, respectively. The thickness contrast clearly shows that the oxide layer formed in H_2O is highly porous with an average pore size of ~ 5 nm after 30 min oxidation (Fig. 3c). In contrast, oxidation in pure O_2 does not lead to the formation of pores in the oxide (Fig. 3b). This indicates vacancy formation and condensation are both enhanced in H_2O. Therefore, water vapour directly influences the alloy oxidation processes in the early stages, which could affect the formation of a protective oxide layer.

Consistent with the water-promoted oxidation as described above is the in situ TEM experimental measurements of oxidation kinetics after the formation of the initial oxide layer. The general process of the oxide growth on Ni–Cr, as shown in Supplementary Fig. 4, features the sparse nucleation and growth of oxide islands on the initial oxide layer. On subsequent oxidation, these oxide islands can reach a few micrometres. By tracking these secondary NiO islands grown on the initial oxide layer, the oxidation rate can be determined directly from in situ observations of the growth process. Two series of time-resolved TEM images (Fig. 4a,b, captured from Supplementary Videos 3 and 4) depict the growth of a single NiO island on a Ni–Cr surface oxidized in H_2O and O_2, respectively. The growth of the large planar oxide island proceeds laterally by rapidly increasing its coverage on the alloy surface. The growth rates of oxide islands in H_2O and O_2 are measured and plotted in Fig. 4c as the cross-sectional area of the growing island versus oxidation
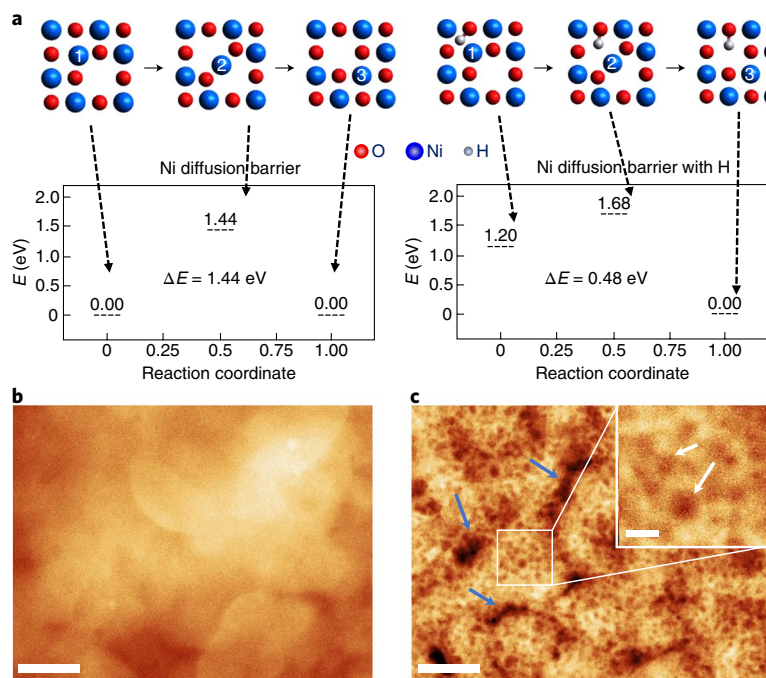
Fig. 3 | Effect of defects on diffusion and microstructure of the oxide layer formed in O$_2$ and H$_2$O. a, DFT-calculated diffusion barrier for Ni in NiO, revealing that the Ni diffusion barrier is changed from 1.44 eV to 0.48 eV if an interstitial H$_i^{\cdot}$ defect is present near the diffusion path as indicated by 1, 2 and 3. **b,c**, STEM-HAADF images, demonstrating a distinctively different structural feature of the initial oxide layer grown on the surface of Ni–Cr alloy in O$_2$ (**b**) and H$_2$O (**c**). The oxide grown in O$_2$ shows a dense structure. The oxide grown in H$_2$O is characterized by a porous structure, where the small dark dots indicate the pores formed by vacancy clustering during the oxidation (white arrows in the inset of **c**). The large dark contrast in **c** (blue arrows) are cavities enclosed by the texture of the alloy thin film and are introduced during the film deposition process. Scale bars, 50 nm (main images, **b** and **c**); 5 nm (inset of **c**).

time. The island growth rates correspond to the slope on the plot of the measured area of the oxide island versus time (Fig. 4c), which denotes 104–306 nm^2 s^{-1} for oxidation in H$_2$O and 24.5–26.8 nm^2 s^{-1} for oxidation in O$_2$. The measured oxidation rate in H$_2$O shows wider scattering than that in O$_2$. This indicates that the oxidation rate also may depend on the transport path for O and Ni, which is affected by the local microstructure (for example, grain boundaries, Cr$_2$O$_3$) of the initial oxide layer. The more porous structure of the initial oxide formed in H$_2$O leads to a relatively large variation in oxide growth rates. However, the general trend is that the growth rate of NiO islands in H$_2$O is higher than that in pure O$_2$.

It is noted that, in terms of defect chemistry, two Cr^{3+} can in principle substitute three Ni^{2+} and create one cation vacancy. However, the Cr doping concentration in NiO is very low, ~0.05%[22], which is far too low to affect the water-induced defect structure. This point is also consistently supported by the oxidation of pure Ni film. We noticed that oxidation of pure Ni in H$_2$O also leads to the formation of vacancy clusters, which does not happen for the case of oxidation in O$_2$ (Supplementary Fig. 19).

In summary, Ni–Cr alloy has been shown to have an enhanced oxidation rate at early stages of oxidation in water vapour environment. Atomic-scale in situ observations provide direct experimental evidence regarding the effect of water vapour on the defect structure and evolution of growing NiO. Water-vapour-promoted oxidation largely stems from the incorporation of interstitial protons (H$_i^{\cdot}$) derived from water dissociation. The dissolved proton in the oxide lowers vacancy formation energy, promotes vacancy clustering, and enhances cation and anion diffusion, all of which leads to an increased oxidation rate in water vapour and consequently a porous structure in the developed oxides at an early stage. The atomic origins of the effect of water vapour on oxidation observed here also provide insights into the mass transport processes of materials in moist environments at elevated temperatures.
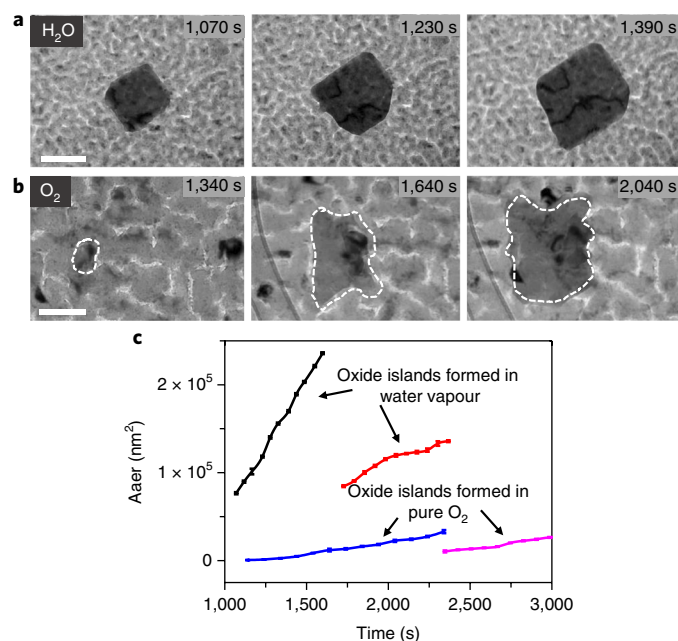

Fig. 4 | Microscale quantification of enhanced oxidation of Ni–Cr alloy in H$_2$O compared to O$_2$. a,b, Time-resolved TEM images depict the growth of large planar NiO islands above the oxide layer formed initially in water vapour (**a**) and oxygen (**b**) ($p = 1 \times 10^{-5}$ mbar and $T = 600\,°C$). The white dashed line in **b** outlines a growing oxide island. Scale bars, 200 nm (**a**); 50 nm (**b**). **c**, Plots of the area of the oxide island as a function of oxidation time, revealing an enhanced oxidation rate in water vapour compared with that in oxygen gas, therefore confirming the effect of water vapour on alloy oxidation at the atomic level.

Methods

Methods, including statements of data availability and any associated accession codes and references, are available at https://doi.org/10.1038/s41563-018-0078-5.

References

1. Steele, B. C. H. & Heinzel, A. Materials for fuel-cell technologies. *Nature* **414**, 345–352 (2001).
2. Eliaz, N., Shemesh, G. & Latanision, R. M. Hot corrosion in gas turbine components. *Eng. Fail. Anal.* **9**, 31–43 (2002).
3. Dutta, R. S. Corrosion aspects of Ni–Cr–Fe based and Ni–Cu based steam generator tube materials. *J. Nucl. Mater.* **393**, 343–349 (2009).
4. Zope, B. N., Hibbitts, D. D., Neurock, M. & Davis, R. J. Reactivity of the gold/water interface during selective oxidation catalysis. *Science* **330**, 74–78 (2010).
5. Douglass, D. L., Kofstad, P., Rahmel, P. & Wood, G. C. International workshop on high-temperature corrosion. *Oxid. Met.* **45**, 529–620 (1996).
6. Saunders, S. R. J., Monteiro, M. & Rizzo, F. The oxidation behaviour of metals and alloys at high temperatures in atmospheres containing water vapour: a review. *Prog. Mater. Sci.* **53**, 775–837 (2008).
7. Hultquist, G., Tveten, B. & Hörnlund, E. Hydrogen in chromium: influence on the high-temperature oxidation kinetics in H_2O, oxide-growth mechanisms, and scale adherence. *Oxid. Met.* **54**, 1–10 (2000).
8. Henry, S., Mougin, J., Wouters, Y., Petit, J. P. & Galerie, A. Characterization of chromia scales grown on pure chromium in different oxidizing atmospheres. *Mater. High. Temper.* **17**, 231–234 (2000).
9. Michalik, M., Hänsel, M., Zurek, J., Singheiser, L. & Quadakkers, W. J. Effect of water vapour on growth and adherence of chromia scales formed on Cr in high and low pO_2-environments at 1000 and 1050 °C. *Mater. High. Temper.* **22**, 213–221 (2005).
10. Essuman, E. et al. Enhanced internal oxidation as trigger for breakaway oxidation of Fe–Cr alloys in gases containing water vapour. *Scri. Mater.* **57**, 845–848 (2007).
11. Zurek, J. et al. Growth and adherence of chromia based surface scales on Ni-base alloys in high- and low-pO_2 gases. *Mater. Sci. Eng. A* **477**, 259–270 (2008).
12. Zhou, G. et al. Step-edge-induced oxide growth during the oxidation of Cu surfaces. *Phys. Rev. Lett.* **109**, 235502 (2012).
13. Li, L. et al. Surface-step-induced oscillatory oxide growth. *Phys. Rev. Lett.* **113**, 136104 (2014).
14. LaGrow, A. P., Ward, M. R., Lloyd, D. C., Gai, P. L. & Boyes, E. Visualizing the Cu/Cu_2O interface transition in nanoparticles with environmental scanning transmission electron microscopy. *J. Am. Chem. Soc.* **139**, 179–185 (2017).
15. Fujita, T. et al. Atomic origins of the high catalytic activity of nanoporous gold. *Nat. Mater.* **11**, 775–780 (2012).
16. Yoshida, H. et al. Visualizing gas molecules interacting with supported nanoparticulate catalysts at reaction conditions. *Science* **335**, 317–319 (2012).
17. Gai, P. L. et al. Visualisation of single atom dynamics in water gas shift reaction for hydrogen generation. *Catal. Sci. Tech.* **6**, 2214–2227 (2016).
18. Zhang, X. et al. Direction-specific van der Waals attraction between rutile TiO_2 nanocrystals. *Science* **356**, 434–437 (2017).
19. Luo, L. et al. In situ atomic scale visualization of surface kinetics driven dynamics of oxide growth on a Ni-Cr surface. *Chem. Commun.* **52**, 3300–3303 (2016).
20. Henderson, M. A. The interaction of water with solid surfaces: fundamental aspects revisited. *Surf. Sci. Rep.* **46**, 1–308 (2002).
21. Norby, T. Protonic defects in oxides and their possible role in high temperature oxidation. *J. Phys. IV Fr.* **03**, C9-99–C99-106 (1993).
22. Atkinson, A. The Role of Active Elements in the Oxidation Behaviour of High Temperature Metals and Alloys: Effect of Active Elements on Diffusion Properties of Synthetic Oxides 55. (Elsevier Science Publishing, New York, NY, 1989).

Acknowledgements

Author contributions

C.W., L.L., D.K.S. and S.M.B. conceived the idea and designed the in situ ETEM experiments. L.L. and P.Y. conducted the in situ ETEM and ex-situ S/TEM analysis. Z.X. and M.S. performed the DFT calculations. L.Z. and G.Z. grew the alloy thin-film samples. D.K.S., D.R.B., Z.Z., Y.W. and S.M.B. discussed the results. L.L., C.W., M.S. and Z.X. wrote the manuscript and all authors have approved the final version.

Competing interests

The authors declare no competing interests.

Additional information

Supplementary information is available for this paper at https://doi.org/10.1038/s41563-018-0078-5.

Reprints and permissions information is available at www.nature.com/reprints.

Correspondence and requests for materials should be addressed to Z.X. or C.W.

Publisher's note: Springer Nature remains neutral with regard to jurisdictional claims in published maps and institutional affiliations.

Methods

Ni–Cr alloy thin-film deposition. Ni–Cr alloy in the form of a single-crystalline 50-nm-thick thin film was deposited on a NaCl substrate at an elevated temperature using a dual-beam electron-beam evaporation system. The concentration of each element was controlled through individual evaporation rate ($9\,\text{Å}\,\text{s}^{-1}$ for Ni versus $1\,\text{Å}\,\text{s}^{-1}$ for Cr), resulting in an atomic ratio ~10 at% of Cr in the Ni–Cr alloy films. Following deposition, the NaCl substrate was removed by water dissolution and the as-deposited alloy thin films were confirmed to be single crystal via electron diffraction.

In situ TEM characterization of Ni–Cr. The oxidation experiments were conducted using a FEI Titan ETEM equipped with an objective-lens aberration corrector. The single-crystalline (100) Ni–10at%Cr alloy thin films (~50 nm in thickness) were washed in acetone and methanol then mounted on a lacey carbon or holey silicon TEM window for observation. The ETEM enabled observation of in situ oxidation with a partial pressure up to a few mbar and at a temperature up to 1,000 °C using a Gatan double-tilt heating holder. Before oxidation, the alloy thin films were annealed at 700 °C in high vacuum $<1\times10^{-8}$ mbar (Supplementary Fig. 5), resulting in a clean surface. Pure oxygen (~99.999%) was introduced into the TEM column through a leak valve to oxidize the thin films at a given temperature and pressure. For oxidation in water vapour, the water vapour was generated and delivered to the ETEM column by a water vapour system developed in-house (schematically shown in Supplementary Fig. 6). A water-containing container was connected through a manifold at one end to a diaphragm pump and to the ETEM inlet at the other end. Initially, the water container valve (V2) was closed, and the pump valve (V1) remained open to pump the pipeline with the diaphragm pump. When the pipeline vacuum reached a few mbar, V1 was closed. Then, V2 was opened to allow the pipeline to fill with water vapour. The vapour pressure of liquid water at 25 °C is ~31.7 mbar, which is substantially larger than the vacuum in the pipeline, allowing the water vapour constantly to evaporate from the liquid water in the container. By repeating this process several times, water vapour of >95% purity was generated as indicated by the analysis result using a residual gas analyser (RGA) located near the sample area in the ETEM column. The gas pressure at the sample is regulated by a computer-controlled leak valve system integrated within the ETEM vacuum and gas delivery control system developed by the ETEM manufacturer (FEI Company, Hillsboro, OR, USA). The gas pressure can be adjusted from 1×10^{-8} to 15 mbar. The cleanliness of the sample was checked by electron diffraction and indicated no additional diffraction spots other than those of the Ni–Cr alloy (Supplementary Fig. 7). A FEI Titan scanning TEM (STEM) equipped with a probe aberration corrector was used to collect ex situ STEM images, and a probe-corrected JEOL ARM 200 STEM equipped with a highly efficient energy dispersive X-ray spectroscopy (EDS) detector was used to analyse the chemical composition of the oxide islands. The electron-beam dose rate was chosen as ~5×10^{4} e nm^{-2} based on calibrations of the electron-beam effect according to established methods[23,24] (detailed in the Supplementary Information).

HRTEM image simulation. To confirm the HRTEM contrast of the vacancy clusters, we used a structure model of NiO with vacancy clusters of five- and three-layer thickness NiO (002) lattice in a $13\times13\times9$ cubic NiO as input to calculate the HRTEM images and compared the simulated image with the experimentally captured image. The multislice method was used to calculate the image, which was integrated into SimulaTEM code (described in ref. [25]). The image simulation

parameters were chosen as follows: accelerating voltage of 300 kV and a spherical aberration coefficient of the objective lens of 2 μm.

Kinetics measurement. The cavity coverage and growth rate of oxide islands was measured by the projected area of the feature versus time from snapshots of the in situ video. Each data point was measured three times, and the error bar is the standard deviation of these measurements.

DFT calculation. DFT calculations were done using the projector-augmented-wave (PAW)[26] methods implemented in the Vienna Ab initio Simulation Package (VASP)[27]. The plane-wave basis set was used, and a cut-off energy of 500 eV was set to ensure a good convergence. Because of the strong correlation nature of NiO, conventional DFT schemes would predict an artificial narrow bandgap for the ground state. Thus, we included the effect Hubbard parameter U_{eff}, also known as the DFT + U method[28]. In our DFT calculations, U_{eff} was chosen to be 4.3 eV for Ni $3d$ orbital[29]. The nudged elastic band (NEB) method[30] was employed to determine the minimum energy path, as well as the saddle point of atomic diffusion. An NiO crystal has a cubic NaCl-type rock-salt structure (space group $Fm\overline{3}m$). A supercell that contained $2\sqrt{2}\times2\sqrt{2}\times3$ 8-atom unit cells (192 atoms) with an antiferromagnetic ground state was used in all calculations. The Brillouin zone integrations were performed using Monkhorst-Pack grids of $2\times2\times2$. All initial structures were fully relaxed until the Hellmann–Feynman force on each ion was smaller than 0.001 eV A^{-1} (0.01 eV A^{-1} in NEB calculations).

Data availability. The data that support the findings of this study are kept at the Environmental Molecular Sciences Laboratory at Pacific Northwest National Laboratory and are available from the corresponding authors on request.

References

23. Gai, P. L. et al. Atomic-resolution environmental transmission electron microscopy for probing gas–solid reactions in heterogeneous catalysis. *MRS Bull.* **32**, 1044–1050 (2007).
24. Gai, P. L., Lari, L., Ward, M. R. & Boyes, E. D. Visualisation of single atom dynamics and their role in nanocatalysts under controlled reaction environments. *Chem. Phys. Lett.* **592**, 355–359 (2014).
25. Gómez-Rodríguez, A., Beltrán-del-Río, L. M. & Herrera-Becerra, R. SimulaTEM: multislice simulations for general objects. *Ultramicroscopy* **110**, 95–104 (2010).
26. Kresse, G. & Furthmüller, J. Efficient iterative schemes for ab initio total-energy calculations using a plane-wave basis set. *Phys. Rev. B* **54**, 11169–11186 (1996).
27. Kresse, G. & Hafner, J. Ab initio molecular dynamics for liquid metals. *Phys. Rev. B* **47**, 558–561 (1993).
28. Dudarev, S. L., Botton, G. A., Savrasov, S. Y., Humphreys, C. J. & Sutton, A. P. Electron-energy-loss spectra and the structural stability of nickel oxide: an LSDA+ U study. *Phys. Rev. B* **57**, 1505–1509 (1998).
29. Yu, J., Rosso, K. M. & Bruemmer, S. M. Charge and ion transport in NiO and aspects of Ni oxidation from first principles. *J. Phys. Chem. C* **116**, 1948–1954 (2012).
30. Henkelman, G., Uberuaga, B. P. & Jónsson, H. A climbing image nudged elastic band method for finding saddle points and minimum energy paths. *J. Chem. Phys.* **113**, 9901–9904 (2000).